Journal of Inorganic and Organometallic Polymers and Materials (2022) 32:2192–2208
https://doi.org/10.1007/s10904-022-02262-8

Ag, Co_3O_4, Ag–Co_3O_4, and Ag/Co_3O_4 Nanoparticles Decorated Mesoporous Natural Phosphate: Effect of Metal Synergy and Preparation Method on the Catalytic Reduction Reaction

Hamza Orfi[1,2] · **Ayoub Abdelkader Mekkaoui**[1,2] · **Buse Sündü**[3] · **Mouhsine Laayati**[1,2] · **Salim Adam Labyad**[1,2] · **Larbi El Firdoussi**[2] · **Önder Metin**[3,4] · **Soufiane El Houssame**[1]

Received: 17 January 2022 / Accepted: 16 February 2022 / Published online: 15 March 2022

Abstract

Addressed herein is a facile method for the preparation of cobalt-silver (Co_x–Ag_y) nanoparticles decorated mesoporous natural phosphate (m-NP). Various Co_x–Ag_y@NP nanocatalysts were prepared in different forms of Ag and Co_3O_4 including mono- and bimetallic active sites. The bimetallic nanocatalysts were prepared by two different preparation methods, namely in-situ (Ag–Co_3O_4) and ex-situ (Ag/Co_3O_4 core–shell). In the first step, colloidal Co_x–Ag_y nanoparticles were synthesized in solution and their formation was monitored by using UV–Visible spectroscopy. Furthermore, the obtained nanoparticles were characterized by XRD and IR spectroscopy. All nanoparticles were deposited on m-NP using a simple wetness impregnation method followed by a calcination at 500 °C. The prepared nanocatalysts were fully characterized by advanced analytical techniques including IR, XRD, XPS, SEM–EDX, FESEM, and TEM. The catalytic reduction of 4-nitrophenol was studied as a model reaction to investigate the effect of synergy created between the metals, oxidation state, catalyst structure, and preparation method on their catalytic activity. Accordingly, reaction kinetics and comparative study of various colloidal Co_x–Ag_y and m-NP supported nanocatalysts in the reduction of 4-nitrophenol was carried out. The optimized conditions were used to study the substrate scope of the catalytic reduction over various nitroarenes.

Keywords Heterogeneous catalysis · Mesoporous natural phosphate · Core–shell nanoparticles · Silver · Cobalt oxide · Nitroarenes

1 Introduction

Monometallic nanoparticles are present in diverse sectors considering their electrical, optical, chemical, or biological applications [1–4]. However, in recent years, bimetallic nanoparticles are highly preferred for various applications due to their unique properties including bi-functionality and synergistic effects between two distinct metal atoms [5–8]. From the catalytic point of view, bimetallic nanoparticles composed of two distinct metals form outstanding catalytically active sites and chemical stability due to the synergistic effects created between the metal atoms [9–12].

Recently, special attention is paid to supported metal nanocatalysts which possess high catalytic performance in terms of the activity and stability. They reveal various benefits compared to their homogeneous counterparts in terms of their practical separation, thermal stability and reusability [12–18]. Consequently, the heterogeneous metal nanocatalysts improve the sustainability of catalytic processes by

---

Hamza Orfi and Ayoub Abdelkader Mekkaoui contributed equally to this study.

✉ Ayoub Abdelkader Mekkaoui
mekk.ayoub@gmail.com

✉ Soufiane El Houssame
hous_soufiane@hotmail.com

[1] Laboratoire des Sciences des Matériaux, Mathématiques et Environnement, Université Sultan Moulay Slimane, Faculté Polydisciplinaire de Khouribga, B.P 145, 25000 Khouribga, Morocco

[2] Equipe de Chimie de Coordination et de Catalyse, Département de Chimie, Faculté des Sciences Semlalia, BP 2390, 40001 Marrakech, Morocco

[3] Department of Chemistry, College of Sciences, Koç University, 34450 Sarıyer, Istanbul, Turkey

[4] Koç University Surface Science and Technology Center (KUYTAM), 34450 Sarıyer, Istanbul, Turkey

converting them into the less time- and energy-consuming ones. Furthermore, anchoring of metal nanoparticles on suitable support materials disclose heterogeneous catalysts possessing high activity and selectivity [15, 16]. Additionally, the deactivation of active sites during chemical processes could be declined or eliminated by using of supported metal nanocatalysts, which results in the longer catalytic lifetime. Moreover, supported metal nanocatalysts boost the catalytic efficiency by increasing the surface area and the support material can improve the catalytic efficiency of the anchored nanoparticles via providing strong support-metal interaction and improved distribution and dispersion, making them more sustainable [19].

Many support materials have been reported so far including metal oxides (Al_2O_3 [20], SiO_2 [14, 21], ZnO [13], CeO_2 [19]), carbon based materials (commercially available carbon blacks [22], carbon nanotubes [23], graphene [24]), natural clays [25], and polymers [26]. However, natural phosphate (NP), which is an attractive and cost-effective catalyst or catalytic carrier for several chemical transformations, has received little attention as a support material for the metal nanoparticles [15, 16], although hydroxyapatite and fluorapatite have been extensively employed in various catalytic applications [27, 28]. Taking into consideration that mesoporous supports allow high distribution and dispersion of active sites, we have recently reported the use of mesoporous NP (m-NP) as a support material for the palladium nanoparticles [15, 16]. According to the characteristic nanosized particles and pores of m-NP, the developed Pd@NP nanocatalysts showed strong catalytic activity, high stability and recyclability in hydrogen transfer reaction [15] and dehydroaromatization of natural olefines [16]. Silver nanoparticles have been found to be more efficient and easily available materials with diverse contributions in various applications [29–31]. The diversity of applications is owing to the tuning of their particle size, shape, surrounding dielectric characteristics, and inter-particle interactions [32]. The potential use of Ag nanoparticles is widely known in catalysis, cancer therapy, electrochemical sensor, drug therapy, and etc. [33]. On the other hand, cobalt and cobalt oxide nanoparticles have also various biomedical applications owing to their distinctive properties [34]. In addition to biomedical applications, they have been widely used in batteries, pigments dyes, electronic thin films, capacitors, and gas sensors [35–37]. In the water electrolysis, Co_3O_4 nanoparticles play a significant role as a catalyst [38]. Moreover, cobalt can exhibit variable oxidation states (Co^{2+}, Co^{3+}, and Co^{4+}) which makes it an attractive transition metal for various catalytic applications. Recently, several eco-friendly, safe, easy, and inexpensive methods has been reported for the synthesis of cobalt and cobalt oxide nanoparticles using a variety of chemical and physical processes [34]. In the last decade, Co-based bimetallic systems has gained considerable importance due to the combined properties of metals coming from their electronic and geometric effects [38, 39]. However, bimetallic cobalt-silver nanoparticles could be deposited on adequate stabilizing supports for a better dispersion and distribution of active sites [40, 41]. Recently, reports are focused on grown cobalt oxide (Co_3O_4) and silver (Ag) nanoparticles on reduced graphene oxide (rGO) as a supercapacitor electrode material [40]. In addition, another Co_3O_4–Ag ternary nanocomposite was carried out through the decoration of fibrous polyaniline as a supercapattery battery-type electrode [41]. According to the literature, numerous studies have been reported on the catalytic performance of Ag/Co_3O_4 bimetallic system [42–44], in contrast there is a lack of studies on Ag–Co_3O_4 supported catalysts. Based on the catalytic performance of supported Co–Ag bimetallic catalysts in selective allylic oxidation of olefins [12–14], we have chosen for the first time to study the mono- and bimetallic Co–Ag nanoparticles supported on m-NP as nanocatalysts.

The reduction of 4-nitrophenol in aqueous solution represents an established "model catalytic reaction" for evaluation of the catalytic activity of metal nanoparticles [45, 46]. In wastewater, nitrophenols and other nitro-derivatives are one of the most common organic contaminants due to their use as herbicides, insecticides, and synthetic dyes [47]. Moreover, they are present in many unexploded landmines worldwide as dangerous high-energy explosives [48]. Additionally, nitro compounds are carcinogenic with genotoxic risks to humans and wildlife [49]. In contrast, the amines that are generally synthesized from the catalytic reduction of nitro compounds play a crucial role as important industrial intermediates. According to the significance of the reduction of nitro compounds, the development of an effective and recyclable catalysts has attracted enormous attention in the chemical industry [50, 51]. Recently, several bimetallic nanoparticles have been studied such as Au–Pt [52], Hg–Pd [53], Pt–Pd [54], Au–Ag [55], Ag–Cu [56], Pd–Co [57, 58], NiPd [59], and FePd [60].

Herein, we report the preparation, characterization, and catalytic application of Co_x–Ag_y nanoparticles supported on m-NP. Several mono- and bimetallic colloidal Co_x–Ag_y nanoparticles in solution and supported on m-NP were prepared and tested as nanocatalysts in the 4-nitrophenol reduction. The deposition was carried out using wetness impregnation method to prepare four types of Co_x–Ag_y@NP supported nanocatalysts. The prepared nanocatalysts were fully characterized and their catalytic performance was evaluated in nitroarene reduction as a model reaction.

2 Experimental

2.1 Materials Synthesis

2.1.1 Preparation of Mesoporous Natural Phosphate

The natural phosphate (NP) was obtained from the region of Khouribga, Morocco [61]. The NP was treated by several techniques involving attrition, sifting, calcinations

(900 °C), washing and re-calcination. After its treatment, the NP has the following chemical composition: CaO (54.12%), P_2O_5 (34.24%), F (3.37%), SiO_2 (2.42%), SO_3 (2.21%), CO_2 (1.13%), Na_2O (0.92%), MgO (0.68%), Al_2O_3 (0.46%), Fe_2O_3 (0.36%), K_2O (0.04%) and numerous trace metals in ppm.

Natural phosphate was subjected to several grinding and sieving as described in our previous studies to obtain a mesoporous support with a particle size of < 45 µm [15, 16]. Due to its nanosized particle size and pores, the m-NP represents a good choice as a catalytic carrier for nanoparticles deposition [15, 16].

2.1.2 Synthesis of Co_x–Ag_y Colloidal Solutions

According to our previously described procedure [15, 16], we have prepared four different types of colloidal Co_x–Ag_y nanoparticles in solution. Typically, monometallic Ag nanoparticles ($x = 0$, $y = 1$), Co nanoparticles ($x = 1$, $y = 0$), in situ Co–Ag nanoparticles ($x = 0.5$, $y = 0.5$) and ex-situ Co/Ag (core/shell) nanoparticles ($x = 0.5$, $y = 0.5$). UV–Visible spectroscopy was used to monitor the formation of all the prepared colloidal Co_x–Ag_y nanoparticle solutions.

2.1.2.1 Synthesis of Monometallic Silver Nanoparticles Colloidal silver nanoparticles in solution were synthesized by (i) mixing in a 500 ml flask a solution of $AgNO_3$ (0.6 mmol) in distilled water (50 ml) with a previously stirred solution of sodium carboxymethylcellulose (CMC-Na, 0.222 g) as a surfactant dissolved in a mixture of water/ethanol (40 ml/10 ml). Then, monodispersed Ag (0) nanoparticles were obtained by (ii) adding an additional amount of water/ethanol (110 ml/ 40 ml) to complete 250 ml of solution mixture under stirring that will be (iii) refluxed for 17 h under air.

2.1.2.2 Synthesis of Monometallic Cobalt Nanoparticles Monodispersed cobalt nanoparticles were synthesized using the same procedure in silver nanoparticles preparation, using $Co(NO_3)_2$,$6H_2O$ (0,6 mmol) as a precursor of cobalt.

2.1.2.3 Synthesis of Bimetallic Co–Ag Nanoparticles The in-situ monodispersed bimetallic Co–Ag colloidal solution was synthesized by (i) mixing and stirring two aqueous solutions (0,3 mmol in 25 ml) of metal precursors $AgNO_3$ and $Co(NO_3)_2 \cdot 6H_2O$. (ii) In a 500 ml flask, the metal precursors solution was mixed with a previously stirred solution of sodium carboxymethylcellulose (CMC-Na, 0.222 g) in a mixture of water/ethanol (40 ml/10 ml). (iii) The volume was completed to 250 ml by adding water/ethanol (110 ml/40 ml) and (iiii) the solution mixture was refluxed for 17 h under air.

2.1.2.4 Synthesis of Bimetallic Co/Ag Core/Shell Nanoparticles First, (i) monodispersed silver nanoparticles were synthesized by the same described procedure. Thereafter, (ii) an aqueous solution of $Co(NO_3)_2 \cdot 6H_2O$ (0.3 mmol in 25 ml) was added to the monodispersed Ag (0) and the mixture was refluxed for 17 h to obtain Co/Ag core/shell nanoparticles.

2.1.3 Deposition of Colloidal Nanoparticles on Mesoporous Natural Phosphate

The solution of as-prepared colloidal nanoparticles (Ag, Co, Co–Ag, and Co/Ag) were used as precursors of nanoparticles deposition on m-NP. The deposition was carried out using simple wetness impregnation procedure by stirring m-NP (0.95 g) in the appropriate colloidal solution followed by 3 h of calcination at 500 °C (Scheme S1). The prepared Co_x–Ag_y@NP nanocatalysts are designed Ag@NP, Co@NP, Co–Ag@NP, and Co/Ag@NP, respectively.

2.2 Materials Characterization

Spectrophotometric analysis of the colloidal solutions was investigated using a double-beam scanning spectrophotometer (Shimadzu spectrophotometer, model biochrom). The stretching vibration frequencies of the obtained nanoparticles and nanocatalysts were recorded by FT-IR spectroscopy in the range of 400–4000 cm^{-1} using a Bruker vertex70 DTGS. Diffraction data were collected at room temperature on a D2 PHASER diffractometer (BRUKER-AXS), with the Bragg–Brentano geometry, using CuKα radiation ($\lambda = 1.5406$ Å) with 30 kV and 10 mA. X-ray photoelectron spectra (XPS) were recorded on Thermo Scientific K-Alpha spectrometer using an Aluminum anode (Al $Ka_{¼}$ 1468.3 eV). The binding energy scale was calibrated by assigning the C 1*s* signal at 284.4 eV. SEM–EDX measurements were obtained with TESCAN VEGA3-EDAX scanning electron microscope equipped with an energy dispersive X-ray detector (EDX). SEM images were acquired by using a Zeiss Ultra Plus Field Emission Scanning Electron Microscope (FESEM). Transmission electron microscopy (TEM) observations were carried out at 120 kV (TEM, Hitachi HT7800 with EXALENS) working at high-resolution (HR) mode with the magnification range of 10–600 k.

2.3 General Procedure for Catalytic Reduction of Nitroarenes

The prepared Co_x–Ag_y@NP nanocatalysts were investigated toward the catalytic reduction of 4-nitrophenol as a catalytic model reaction and their substrate scope was investigated on other nitroarenes. A typical reaction was carried out in a round bottom flask at room temperature, by adding an aqueous solution of $NaBH_4$ ($2.2*10^{-1}$ M) as hydrogen source and the aqueous solution of 4-nitrophenol ($3.5*10^{-3}$ M) in presence of Co_x–Ag_y@NP (catalyst/substrate = 35% wt.). The catalytic reduction was monitored by UV–Visible spectroscopy showing the decrease of absorbance at 400 nm related to 4-nitrophenolate (obtained after the addition of $NaBH_4$) and the revelation of a new band at 300 nm indicating the formation of 4-aminophenol. The optimized conditions were used to study the reaction kinetics in presence of various colloidal Co–Ag nanoparticles and m-NP supported nanocatalysts. The recyclability of the optimum prepared nanocatalysts was carried out. Furthermore, the same conditions were used in the reduction of various nitroarenes. The resulting products were extracted from the aqueous medium and the obtained organic phase was analyzed by gas chromatography.

3 Results and Discussion

3.1 Materials Characterization

3.1.1 Colloidal Co_x–Ag_y Nanoparticles

The UV–Visible spectra of as-prepared Co_x–Ag_y colloidal nanoparticles (Fig. 1) show a wide absorption band around $\lambda_{max} = 420$ nm attributed to surface plasmon resonance (SPR) band of Ag nanoparticles (Ag, Co–Ag, and Co/Ag). In contrast to monometallic Ag nanoparticles, the bimetallic Co_x–Ag_y nanoparticles show an additional band around 280 nm that could be assigned to the formation of silver oxide species [23, 62]. Moreover, the silver oxide absorbance was significant compared to SPR band in the case of Co/Ag core–shell nanoparticles. While the in-situ Co–Ag nanoparticles, represents an important SPR absorbance as well as a moderate intensity of silver oxide band. However, the absorbance band around 310 nm in the UV–Visible spectra of colloidal Co and Co–Ag nanoparticles can be attributed to the presence of Co(II) species [63]. As a result of the UV–Visible spectra, we can conclude that ex-situ colloidal solution (Co/Ag) promotes the formation of silver oxide compared to in-situ one (Co–Ag) with absence of cobalt band due to the core/shell structure.

The FT-IR spectra of the as-prepared Co_x–Ag_y nanoparticles and sodium carboxymethylcellulose (CMC-Na) present some slight differences compared to the reference CMC-Na (Fig. 2a), due to the formation of CMC-M (where M = Co_x–Ag_y) in colloidal solutions by the possible interactions between CMC and metal nanoparticles. However, the FT-IR spectra (Fig. 2b) of the obtained nanopowders after purification with washing with distilled water and acetone, confirm the synthesis of pure CMC-M nanoparticles structure (M = Ag; Co; Co–Ag; and Co/Ag). The vibration stretching of the significant band around 3445 cm^{-1} is attributed to the O–H group of molecular water and O–H groups. Hence, the noticeable increasing of this band intensity (3445 cm^{-1}) indicates the formation of cobalt hydroxide species (Fig. 2b_1) [64–66]. Furthermore, two main bands at 506 cm^{-1} and 805 cm^{-1} are related to the metal–oxygen and the metal-OH bending vibrations (δ(Co–O–H) and γ(Co–O)) with additional bands related to Co–OH at 1059 cm^{-1}, 1097 cm^{-1}, 1263 cm^{-1}, 1384 cm^{-1}, and 1636 cm^{-1}, coming from $Co(OH)_2$ formation [67–70]. On the other hand, the slight absorption band around 580 cm^{-1} that appears in Co–Ag and Co/Ag samples can be attributed to Ag–O stretching mode, which corresponds to a slight presence of

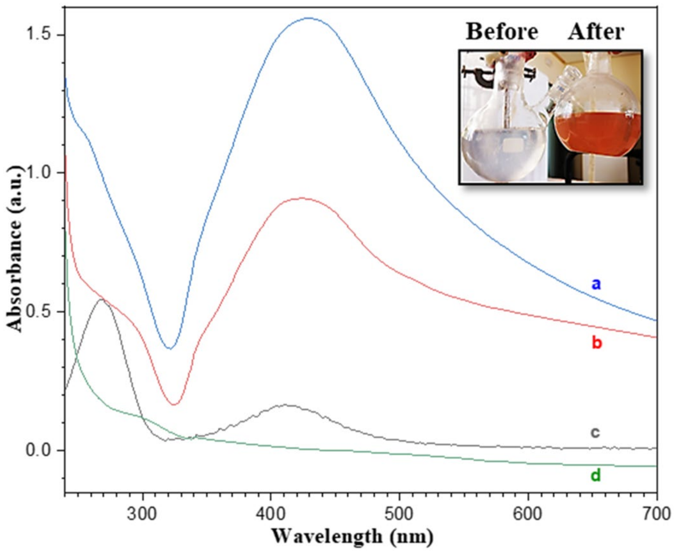

Fig. 1 UV–Visible spectra of colloidal solutions of as-prepared Co_x-Ag_y nanoparticles **a** Ag, **b** Co–Ag, **c** Co/Ag, and **d** Co stabilized by CMC

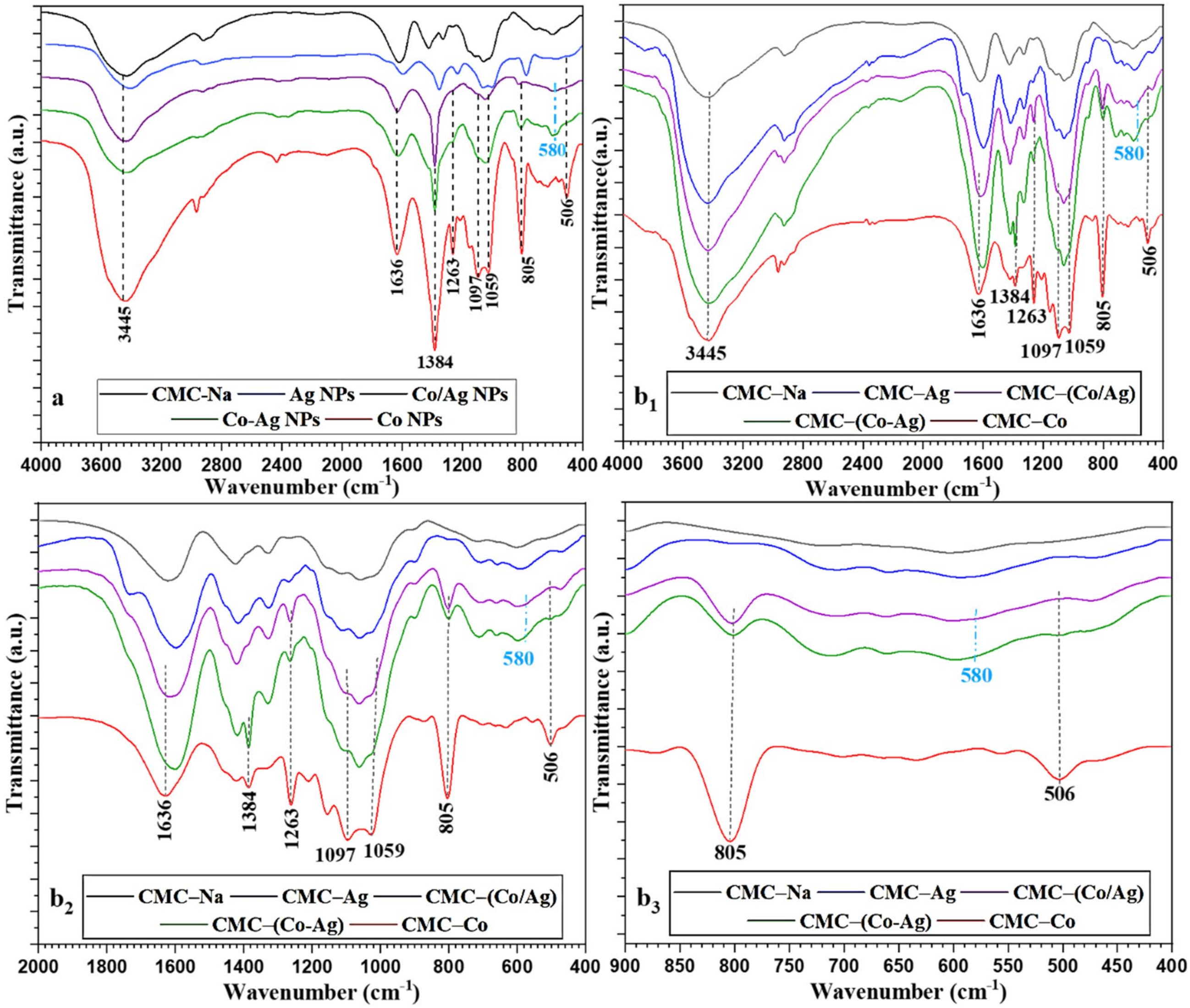

Fig. 2 FT-IR spectra of pure CMC-Na and **a** all as-prepared nanoparticles stabilized by CMC and **b** pure CMC-M (M = Ag; Co; Co–Ag; and Co/Ag) nanoparticles after purification

silver oxide in bimetallic Co_x–Ag_y nanoparticles [71]. The absence of this band in the monometallic Ag nanoparticles confirms the complete reduction of silver precursors to Ag (0), in consistence with UV–Visible spectra. All FT-IR bands of monometallic Ag nanoparticles sample are attributed to CMC-Ag structure owing to the interaction with the silver metallic species.

XRD analyses of the as-prepared nanoparticles indicate the presence of intense peak at 2θ = 29.4° indexed to (104) plane of $NaNO_3$ phase in all samples (Fig. S1). The presence of $NaNO_3$ can be explained by its formation during the interaction between CMC-Na and metal precursors $M(NO_3)_x$, which confirms the FT-IR results of CMC-M formation. However, the XRD spectra of the obtained nanopowders after purification, designed CMC-M (M = Ag; Co; Co–Ag; and Co/Ag), reveal the presence of Ag, Ag_2O, $Co(OH)_2$, and Co patterns (Fig. 3). We have noticed the presence of peaks located at 2θ = 18.07°, 32.15°, 38.04°, and 39.27°, which can be indexed to (001), (010), (011), and (002) planes of hexagonal $Co(OH)_2$ (JCPDS 96-101-0268), with crystallite size of 39.92, 34.76, 20.23, and 24.47 nm, respectively for CMC-Co (Fig. 3). Furthermore, the presence of Ag (0) nanoparticles was also confirmed by the wide peak around 2θ = 38°, which is readily assigned to (111) plane of face centered cubic metallic silver (JCPDS 96-150-9147), with crystallite size of 2.15, 3.76, and 5.34 nm for CMC-Ag, CMC-(Co–Ag), and CMC-(Co/Ag) respectively. In addition to Ag (0), the XRD spectra show the presence of cubic phase of Ag_2O (JCPDS 41-1104) around 2θ = 27.8°, 32.2° and 46.2° indexed to (110), (111), and (211), with crystallite size of 34.41, 40.97, and 42.8 nm for CMC-(Co–Ag) and 34.64, 13.12, and 36.56 nm for CMC-(Co/Ag) respectively. In addition, the bimetallic Co–Ag and Co/Ag nanoparticles point out a remarkable absence of the intense pattern at 2θ = 18.07° related to $Co(OH)_2$, with presence of Ag_2O phase which present intense patterns in the case of core–shell nanoparticles. Although, the same patterns could be attributed to $Ag_xCo_{3-x}O_4$ phase [72]. Accordingly, the observed patterns attributed to Ag, Ag_2O, and $Co(OH)_2$ phases are in good agreement with the UV–Visible and FT-IR results.

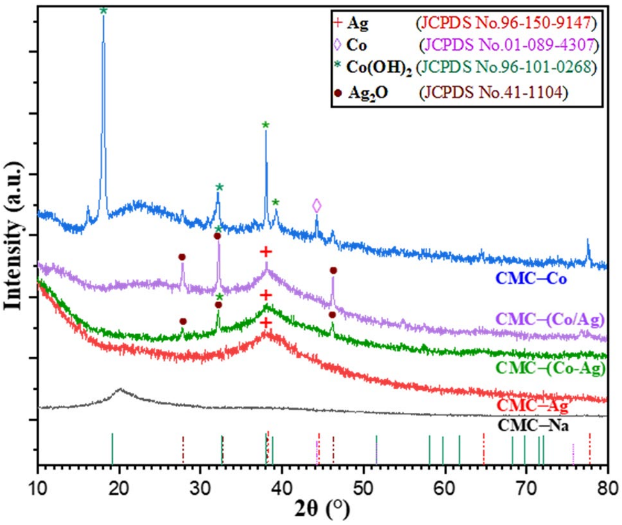

Fig. 3 XRD spectra of CMC-Na and obtained CMC-M (M = Ag; Co; Co–Ag; and Co/Ag) nanoparticles after purification

3.1.2 Co_x–Ag_y@NP Nanocatalysts

The deposition of Co_x–Ag_y nanoparticles on m-NP was carried out using a simple wetness impregnation method followed by calcination at 500 °C for 3 h. The FTIR spectra of m-NP and Co_x–Ag_y@NP nanocatalysts indicate the stability of the crystalline apatite after deposition and reveal the characteristic bands of phosphate groups at 560–600, 960, and 1030–1120 cm^{-1} (Fig. S2).

The crystallite structure of the as-deposited Co_x–Ag_y nanoparticles on the surface of m-NP was studied by XRD analysis. All the patterns of the prepared Co_x–Ag_y@NP nanocatalysts were not the same compared to the support m-NP (Fig. 4). The peaks appearing at 2θ = 38.46° and 44.39° are indexed to (102) and (110) planes of face centered cubic metallic silver, respectively, confirming the deposition of Ag (0) nanoparticles on m-NP for the prepared nanocatalysts Ag@NP, Co–Ag@NP and Co/Ag@NP. By using the wide peak at 2θ = 38.46°, the crystallite size of silver was calculated to be 53.40 nm, 22.88 nm, and 29.12 nm, respectively. However, the XRD patterns of Co@NP, Co–Ag@NP and Co/Ag@NP confirm the presence of Co_3O_4 indicated by the peak at 2θ = 46.92°, which can be assigned to (400) plane of cubic phase of the spinel Co_3O_4 [73]. According to the Scherrer equation [74], the crystallite size of Co_3O_4 were respectively 27.50, 37.20 and 27.49 nm. On the other hand, XRD region of natural phosphate shows a significant shifting of apatite peaks both in the deposition of monometallic and bimetallic cobalt nanoparticles (Fig. 4b). While the slight shifting of Co@NP patterns may be due to Co_3O_4 deposition on m-NP surface, the significant shifting for Co–Ag nanocatalysts could be attributed to the presence of

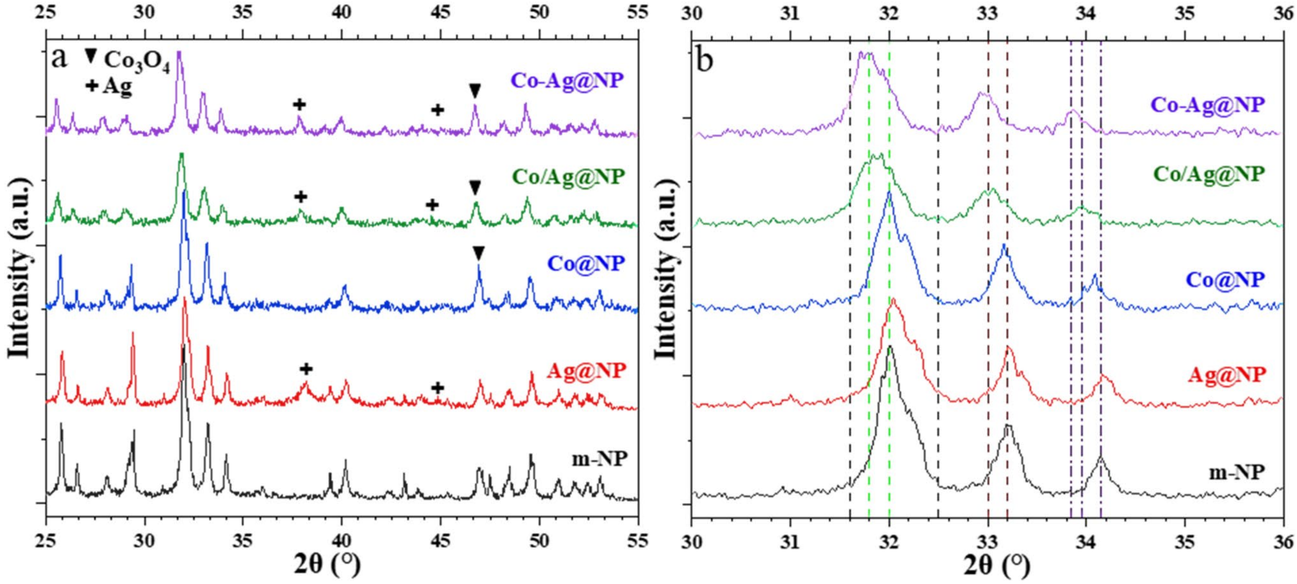

Fig. 4 XRD patterns of m-NP and the prepared Co_x–Ag_y@NP nanocatalysts

silver oxide on the surface. In addition, the shifted peaks of Co–Ag@NP and Co/Ag@NP nanocatalysts (Fig. 4b) might be related to the intercalation with silver oxide peaks Ag_2O (111) and AgO (111) at $2\theta = 32.3°$ and 34.1°, respectively (JCPDS 12-0793 and JCPDS 84-1547) [75]. The presence of silver oxide species was detected in bimetallic nanoparticles analysis and could be also explained by the metallic redox interaction during the calcination process [76, 77].

The observed shifting of the characteristic XRD peaks of the natural apatite leads us to study the lattice parameters and the crystallite sizes of m-NP before and after deposition of Co_x–Ag_y nanoparticles (Table S1). The lattice parameters indicates that the deposition of Co_x–Ag_y nanoparticles does not have a significant effect on the crystalline system of the apatite support with a slight difference on lattice parameters for the bimetallic nanocatalysts. However, the used colloidal solutions for the deposition of these nanoparticles shows an improvement resulting in a decrease of m-NP crystallite size. Moreover, the deposited bimetallic nanoparticles show interesting results especially for the deposited Co/Ag core–shell nanoparticles.

To understand the exact local electronic and chemical configuration of the deposited Co_x–Ag_y nanoparticles on m-NP, XPS analyses were carried out. The chemical environment and the oxidation state of silver and cobalt were studied through the Ag 3*d* and Co 2*p* regions (Figs. 5 and 6). In addition to the representative elements of m-NP (phosphate, calcium, oxygen, fluor, and carbon), all XPS survey spectra confirm the deposition of Co_x–Ag_y nanoparticles in the prepared Co_x-Ag_y@NP nanocatalysts (Figs. 5 and 6a–d).

The XPS spectrum of monometallic Ag@NP nanocatalysts indicates that the deposited silver nanoparticles are in metallic form (Fig. 5a and a_1). While the major Ag $3d_{5/2}$ component is centered at binding energy (BE) of 367.39 eV and the second spin–orbit pair of minor intensity Ag $3d_{3/2}$ is detected at BE of 373.16 eV. The Ag $3d_{5/2}$ and Ag $3d_{5/2}$ are presented as a doublet with spin orbit split of ≈ 6 eV, which is in a good agreement with the characteristic data of metallic silver [78]. On the other hand, the monometallic nanocatalyst Co@NP shows two separated peaks, Co $2p_{3/2}$ at BE of 779.68 eV and Co $2p_{1/2}$ at BE of 795.05 eV with a characteristic spin–orbit split of 15.37 eV (Fig. 6b and b_1). The Co 2*p* XPS spectrum indicates that the cobalt is deposited as Co_3O_4 [79].

The XPS spectra of both Co–Ag@NP and Co/Ag@NP nanocatalysts were studied too (Figs. 5 and 6c, c_1, c_2, d, d_1 and d_2). The Ag 3*d* spectra of the deposited bimetallic nanoparticles were rather different from monometallic silver one. In addition to the main existence of metallic Ag, the bimetallic Co–Ag@NP shows a minor presence of Ag/Ag_2O mixed phase noticed by Ag $3d_{5/2}$ (365.1 eV) and Ag $3d_{3/2}$ (370.64 eV) peaks [75]. In contrast, the metallic silver represents a minor phase for the deposited bimetallic core–shell nanoparticles, due to the major presence of AgO species confirmed by Ag $3d_{5/2}$ (370.65 eV) and Ag $3d_{3/2}$ (376.64 eV) [80]. The Co 2*p* spectra of Co–Ag@NP and Co/Ag@NP nanocatalysts, present the same results observed for cobalt monometallic deposition indicated by the presence of $2p_{3/2}$ and $2p_{1/2}$ peaks and two satellite peaks (Fig. 6c_2 and d_2), which is in good agreement with Co_3O_4 XPS spectra [79].

In order to study the effect of nanoparticles deposition on the structural and electronic chemical configuration of the support material, XPS analyses of all prepared nanocatalysts were also studied for major elements in m-NP structure (P 2*p*, O 1*s*, Ca 2*p*, F 1*s*, and C 1*s*) (Fig. S3). The P 2*p* spectrum shows the typical P $2p_{3/2}$ peak of natural phosphate at BE of 133.2 eV with a slight difference in the electronic configuration for bimetallic nanocatalysts and especially a significant shifting observed for bimetallic Co/Ag core/shell nanoparticles. These results indicated the interactions of the deposited bimetallic nanoparticles with the phosphate group in the natural apatite. While O 1*s* presents mainly two peaks attributed to $PO_4^{3-} + OH^-$ and O^{2-}, with the same remarked peak position modification for bimetallic deposition may be due to the deposition of silver oxide nanoparticles in the surface. The binding energy of Ca $2p_{3/2}$ and Ca $2p_{1/2}$ matches those reported in the literature for natural phosphate [81]. The differentiation in Ca 2*p* spectrum for deposited Co/Ag core/shell nanoparticles could be attributed to the interaction of calcium groups with the deposited silver oxide in the surface of m-NP. The spectra of F 1*s* (684.9 eV for NP) confirm the fluorapatite aspect of the m-NP used as a support for the deposition of nanoparticles. The C1s spectra confirmed the presence of carbonate in m-NP with the same noticed spectrum modification for the core–shell deposition due to the interaction of metallic nanoparticles with the support.

The analysis of XPS spectra of main m-NP elements showed no-significant modification in terms of electronic and chemical configurations for monometallic deposition on m-NP surface. In contrast, the bimetallic deposition reveals some modifications due to the presence of silver oxide species (AgO and Ag_2O) and to the important interaction of bimetallic Co_x-Ag_y nanoparticles with the m-NP surface, especially for deposited Co/Ag core/shell nanoparticles.

To investigate the morphology, the dispersion, and the distribution of the deposited Co_x-Ag_y nanoparticles on m-NP, FESEM images were recorded for all prepared Co_x-Ag_y@NP nanocatalysts (Fig. 7). The FESEM images indicated that nanoparticles deposition has no effect on the m-NP morphology (Fig. 7a_1, b_1, c_1 and d_1). The monometallic deposition of silver nanoparticles formed well dispersed and distributed nanospheres on the surface Fig. 7a_2 and a_3). The deposited nanospheres were identified as formed Ag@NP nanocomposites on m-NP surface as showed by EDX and elemental mapping analysis (nanosphere composed by Ag and major m-NP (fluorapatite) elements) (Fig. 8). On

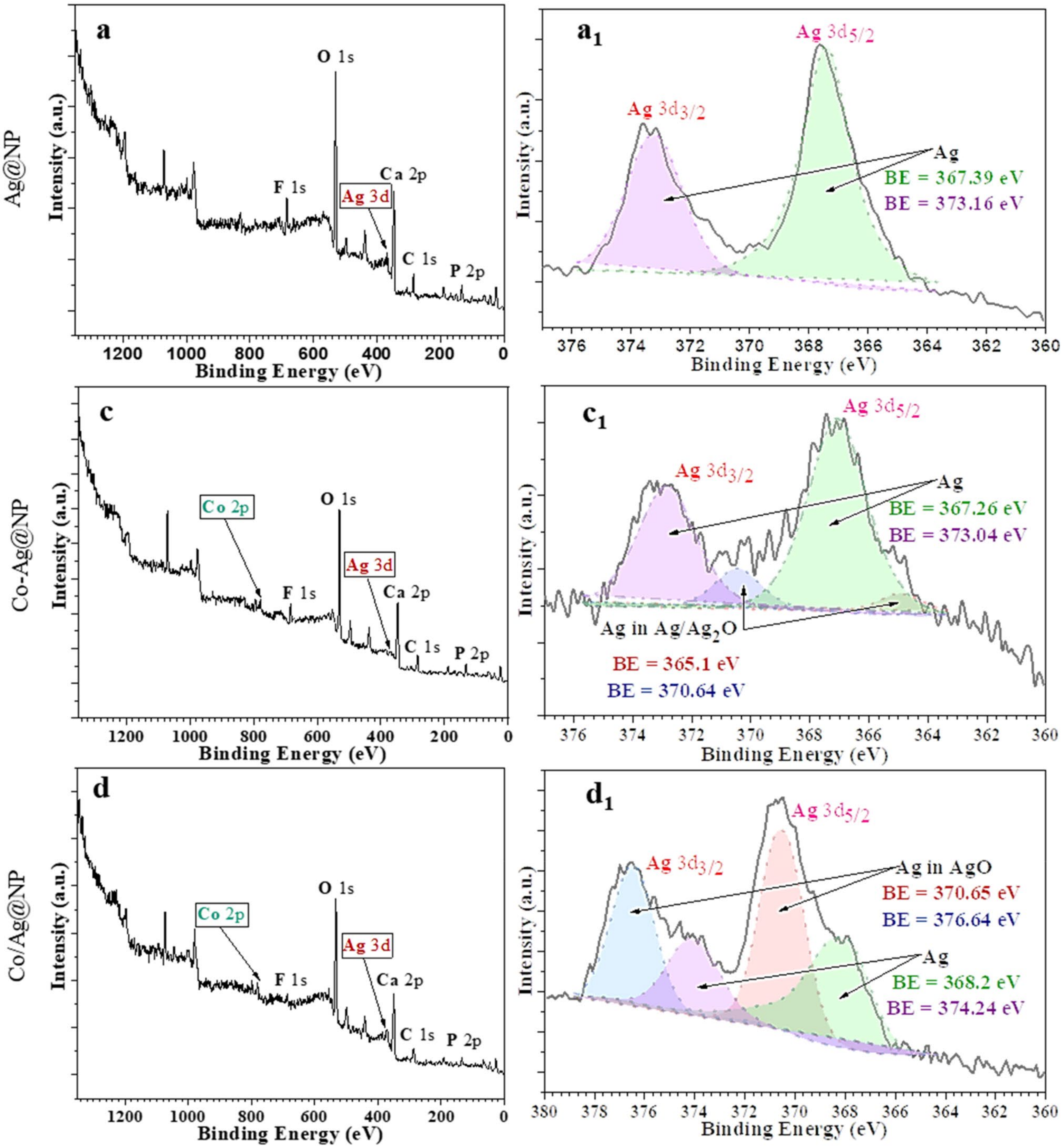

Fig. 5 XPS spectra of deposited silver nanoparticles for **a** Ag@NP, **c** Co–Ag@NP and **d** Co/Ag@NP nanocatalysts

the other hand, the deposition of cobalt leads to distributed Co_3O_4 nanograins on the mesoporous NP surface (Fig. 7b$_2$ and b$_3$). In contrast, the bimetallic nanocatalysts show different results compared to monometallic deposition (Fig. 7c and d). Both in-situ and ex-situ Co_x-Ag_y colloidal solutions lead to the deposition of distributed silver nanospheres decorated Co_3O_4 nanograins (Fig. 8c$_3$ and d$_3$). In case of Co/Ag core/shell deposition, a slight differentiation in terms of dispersion and distribution is noticed for the obtained silver decorated Co_3O_4 (Fig. S4).

TEM analyses were carried out to explore the shape and size of the deposited nanoparticles on m-NP (Fig. 9). The TEM images of the monometallic Ag nanoparticles deposited on m-NP showed a well-dispersed nanoparticles with

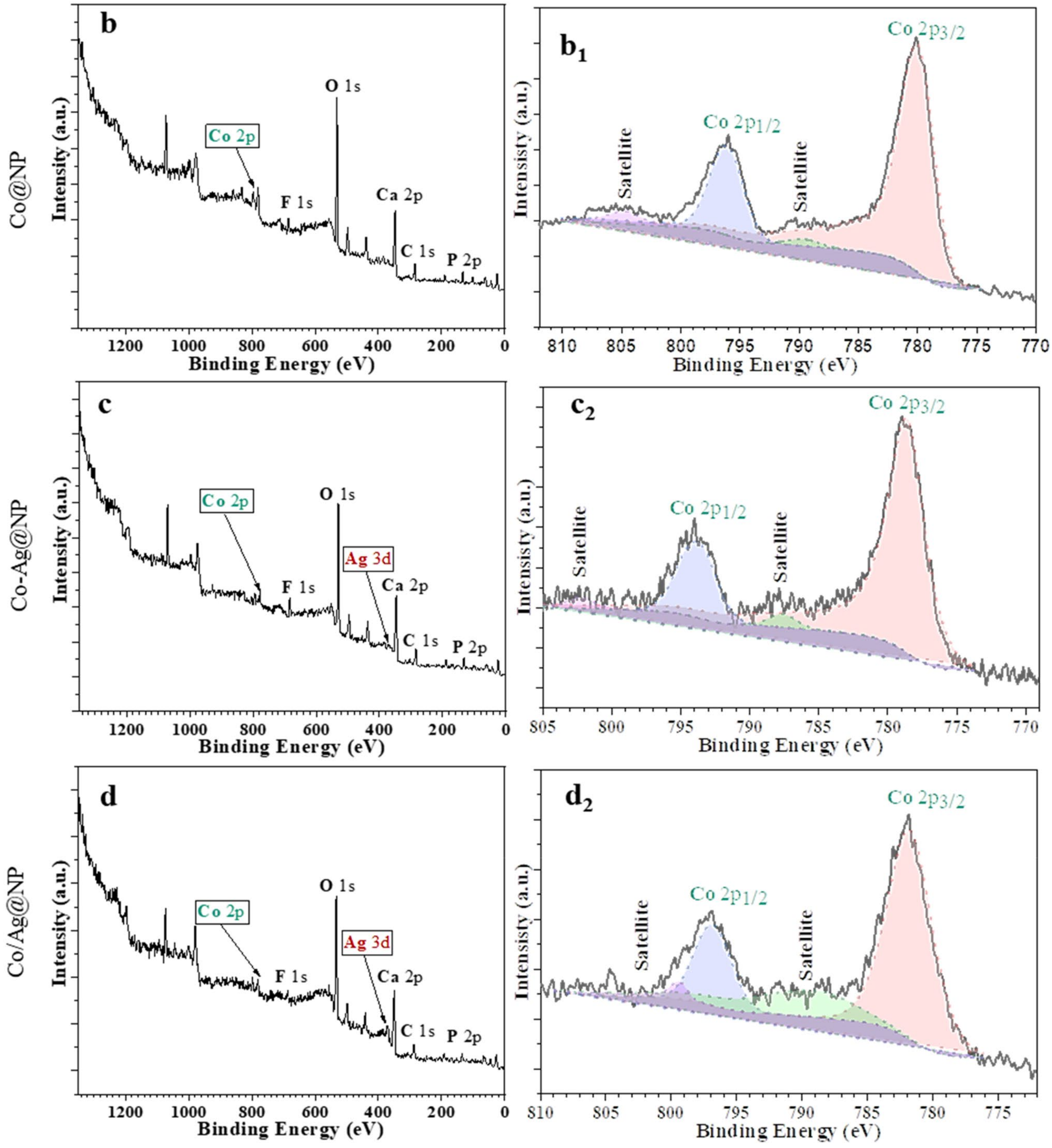

Fig. 6 XPS spectra of deposited Co_3O_4 for **b** Co@NP, **c** Co–Ag@NP and **d** Co/Ag@NP nanocatalysts

an average particle size of 10 nm, and confirm the observed Ag@NP nanospheres by FESEM-EDX analyses (Fig. 9a). In the case of the monometallic deposition of cobalt, the images revealed the presence of chain-like (deposited nanograins observed by FESEM) and cubic Co_3O_4 nanoparticles deposited on m-NP surface (Fig. 9b). The deposition of in-situ colloidal solution of Co_x–Ag_y exhibits the decoration of m-NP support by both Ag and Co_3O_4 nanoparticles possessing good distribution and well-dispersion (Fig. 9c). In contrast, the deposition of ex-situ Co_x–Ag_y colloidal solution exhibits the presence of Co/Ag core/shell nanoparticles formed mainly by Co_3O_4 nanograins (core) decorated by Ag nanospheres and silver oxide film (shell) (Fig. 9d).

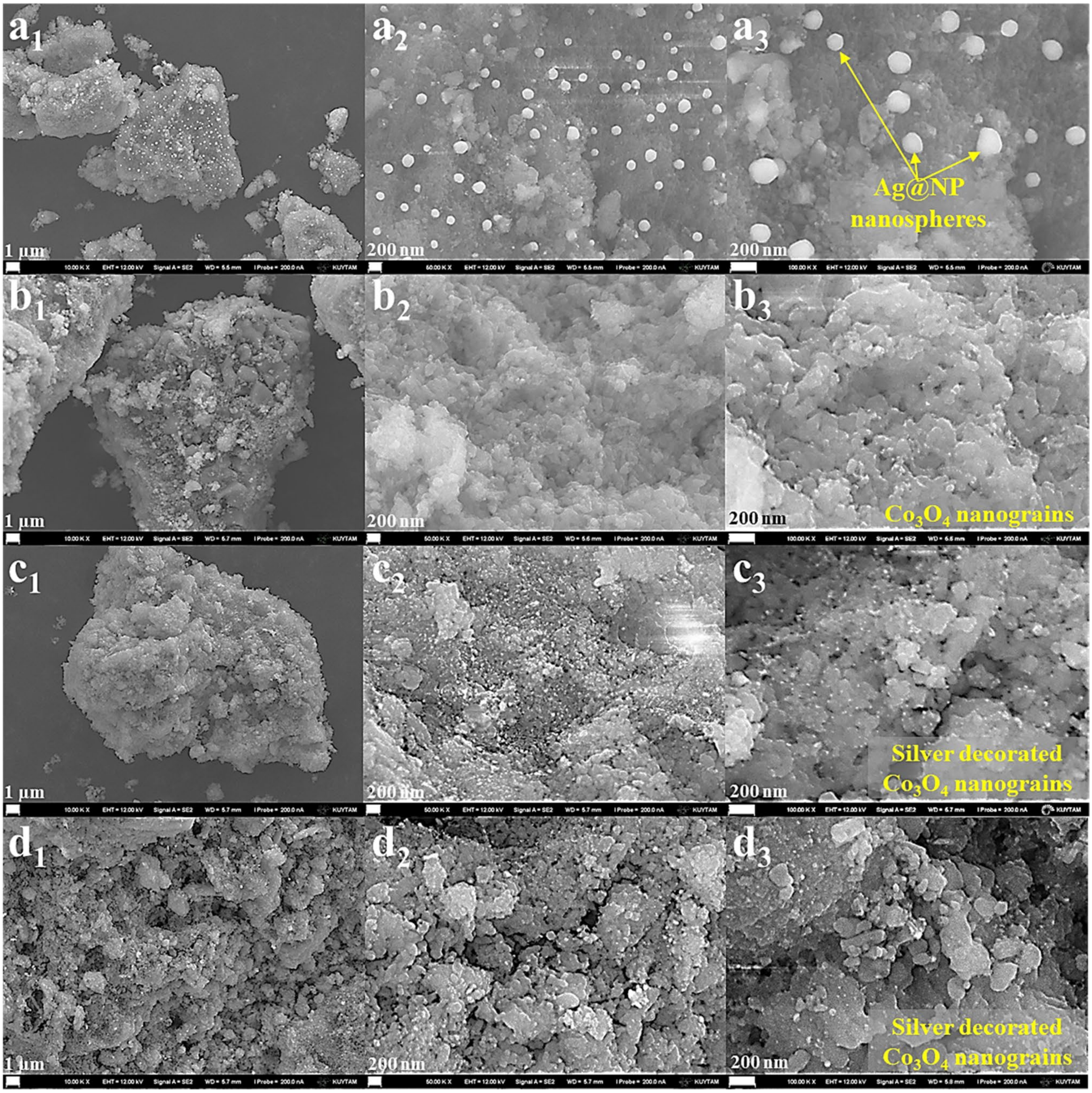

Fig. 7 FESEM images of **a** Ag@NP, **b** Co@NP, **c** Co–Ag@NP, and **d** Co/Ag@NP nanocatalysts

3.2 Catalytic Application

3.2.1 Catalytic Reduction of 4-Nitrophenol

The catalytic activity of Co_x–Ag_y@NP nanocatalysts was evaluated for the reduction of 4-nitrophenol (4-NP) as a well-accepted model reaction. The reduction reactions were carried out using $NaBH_4$ as reducing agent in aqueous medium under ambient conditions (Fig. S5). The direct reduction of 4-NP by $NaBH_4$ is thermodynamically feasible but kinetically restricted due to the lack of an efficient catalyst [82]. The catalytic transformation is simple and very fast with the advantage of monitoring the reduction by UV–visible spectroscopy. The use of mesoporous natural phosphate alone cannot catalyze the catalytic reduction of 4-NP.

In presence of $NaBH_4$, the 4-nitrophenol is converted to 4-nitrophenolate ion which is noticed by the change of color from light yellow to bright yellow, and the absorption peak shifting from 317 to 400 nm (Fig. 10a). After

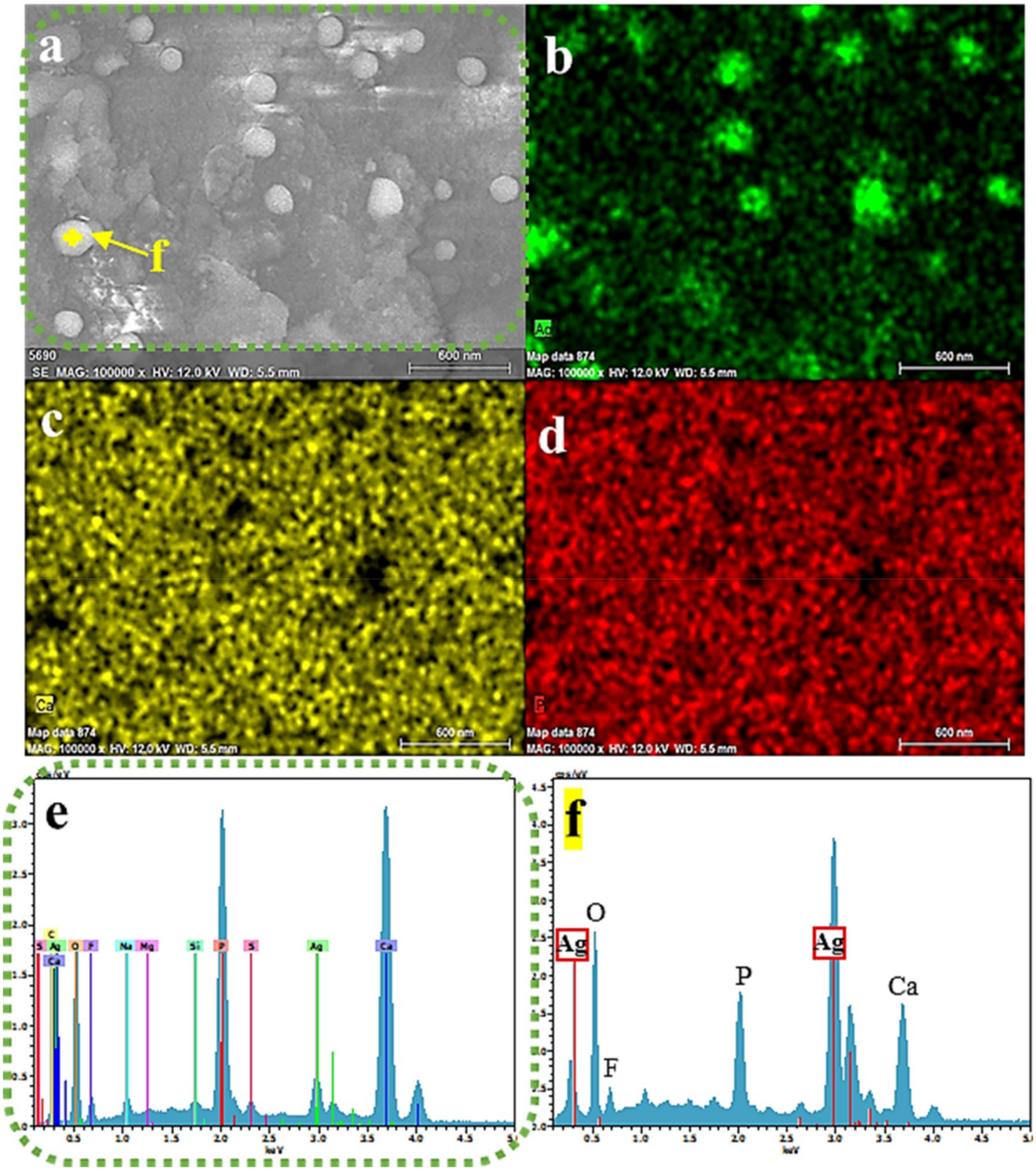

Fig. 8 EDX and elemental mapping analyses of Ag@NP nanocatalyst: **a** studied area, **b** Ag mapping, **c** Ca mapping, **d** P mapping, **e** EDX of studied area, and **f** EDX of Ag@NP nanospheres

addition of the catalyst, the characteristic absorption peak of 4-nitrophenolate at 400 nm started to decrease while a new absorption band at 300 nm appeared due to 4-aminophenol formation (Fig. 10b). In addition, the change in the color of reaction mixture from bright yellow to colorless solution was also an indication of the catalytic reduction of 4-NP (Fig. S5). The comparison of Co_x–Ag_y@NP catalytic performances indicate that deposited silver nanoparticles (Ag@NP) are more efficient compared to Co_3O_4 (Co@NP). However, the bimetallic Co_x–Ag_y nanocatalysts reveal a great improvement in catalytic activity in comparison to monometallic Ag@NP nanocatalyst. These results reveal the great effect of bimetallic synergy on the catalytic performance. On the other hand, the deposited Co–Ag nanoparticles gave better catalytic activity than the Co/Ag ones. The less catalytic efficiency in terms of reaction kinetics of Co/Ag@NP nanocatalyst could be due to the presence of silver oxide film on the deposited core–shell nanoparticles. In contrast, Co–Ag@NP presents a uniform distribution of Co_3O_4 and Ag NPs

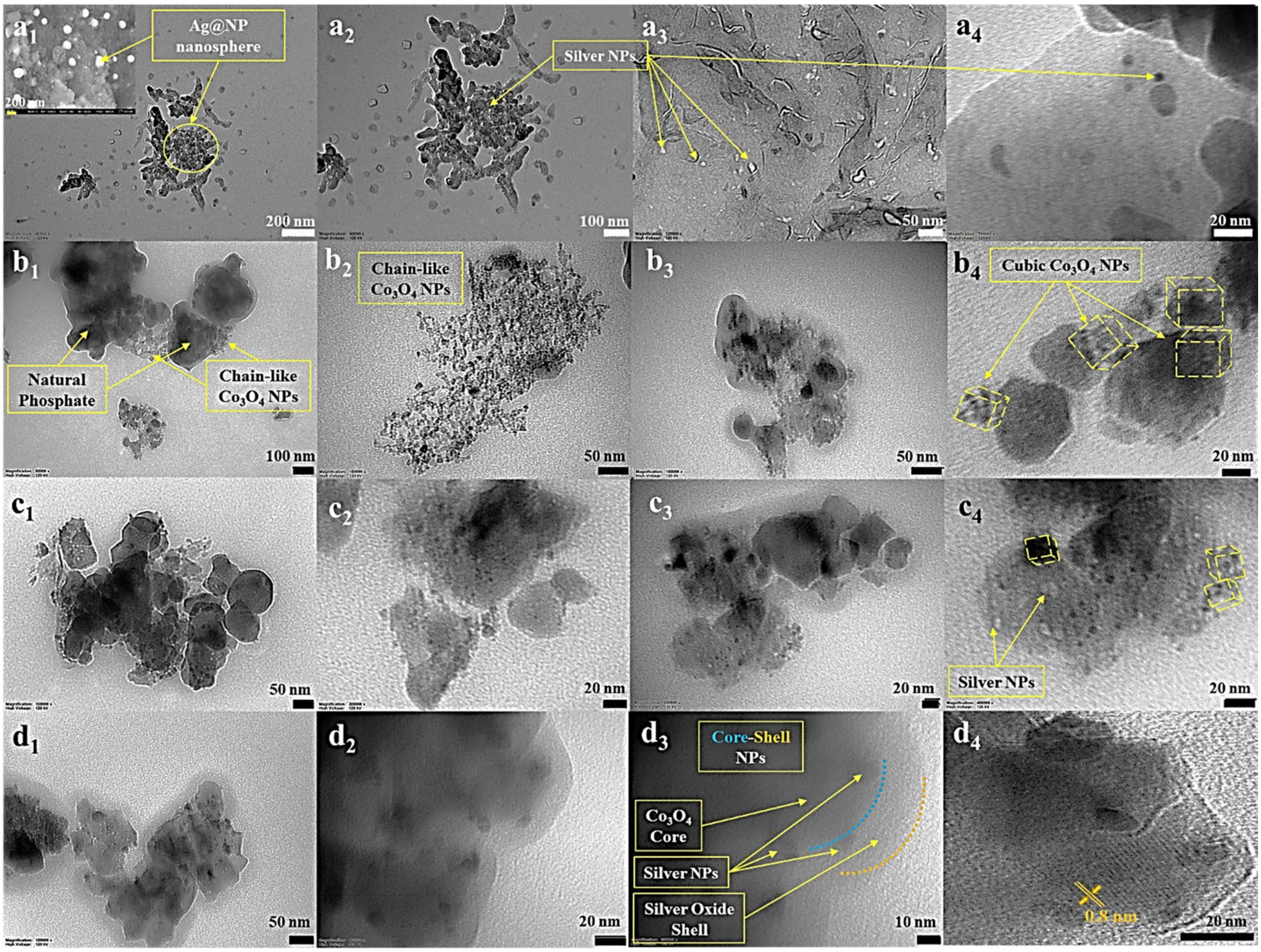

Fig. 9 TEM images of **a** Ag@NP, **b** Co@NP, **c** Co–Ag@NP, and **d** Co/Ag@NP nanocatalysts

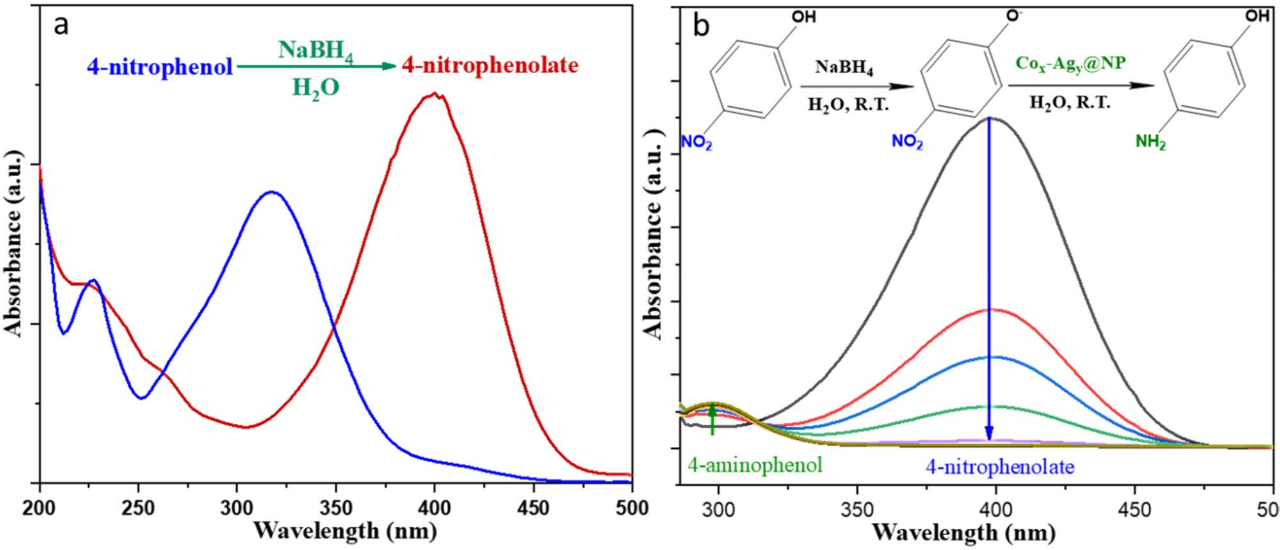

Fig. 10 General presentation of UV–Visible spectra of **a** 4-nitrophenol transformation to 4-nitrophenolate in presence of $NaBH_4$ and **b** catalytic reduction of 4-nitrophenolate to 4-aminophenol catalyzed by Co_x–Ag_y@NP

(See Fig. 9). Furthermore, XPS spectra show silver oxide as predominant oxidation state compared to Co–Ag@NP where metallic silver is mainly the dominant specie. The fact that metallic silver is the highly active catalytic specie can explain the catalytic performance of Co–Ag@NP compared to Co/Ag@NP. Consequently, Co–Ag@NP was chosen as a model nanocatalyst to optimize the 4-NP catalytic reduction.

The catalytic activity of 4-NP was investigated with various amount of $NaBH_4$ (0.036 to 0.392 M) to determine the optimal concentration of the reducing agent, in presence of Co–Ag@NP (Catalyst/Substrate = 50% wt.) as the model nanocatalyst. The reaction time was dependent on $NaBH_4$ concentration with no effect on 4-NP conversion, which indicate a high catalytic efficiency of the model nanocatalyst. Due to the presence of $NaBH_4$ excess, the catalytic transformation rate was assumed to be dependent only on the substrate, which can be fitted using a first-order rate law to 4-NP concentration. During the optimization, the kinetic of each catalytic reaction has been studied following the reaction rate constant (k) calculated using $\ln(A_t/A_0) = -kt$, where A_t and A_0 represent the absorbance at 400 nm at time t and 0 (Fig. 11). The regular use of $NaBH_4$ excess in such catalytic transformation could be explained by the increase of produced BH_4^- ions which facilitate the catalytic hydrogen transfer process to convert 4-NP to 4-AP.

The effect of catalyst amount on the catalytic reduction of 4-NP was investigated using various catalyst/substrate ratio (10 to 50% wt.) of Co–Ag@NP chosen as the model nanocatalyst. The best result was obtained with 0.221 M $NaBH_4$ concentration (Fig. 12). The total catalytic reduction of 4-NP takes place from a moderate to a fast time. With a small catalytic ratio of 10%, the total conversion of 4-NP with a reaction time of 65 min indicates the efficiency of the developed Co–Ag@NP nanocatalyst. Starting from catalyst/substrate ratio of 30%, high constant rate was obtained with a shorter reaction time. The ratio of 35% was the best optimum amount for the catalytic application with 98% of conversion in 11 min and a rate constant of 0.4542 min^{-1}.

3.2.2 Substrate Scope and Limitations of Catalytic Reduction of Nitroarenes in Presence of Co–Ag@NP Nanocatalysts

The scope and limitations of the developed nanocatalytic system were investigated in the reduction of several other nitroarenes under the optimized conditions. As shown in Table 1, all studied nitroarenes bearing electron withdrawing or donating substituents were converted to the corresponding amino products in a shorter reaction time compared to previously published nanocatalyst Pd@NP [15].

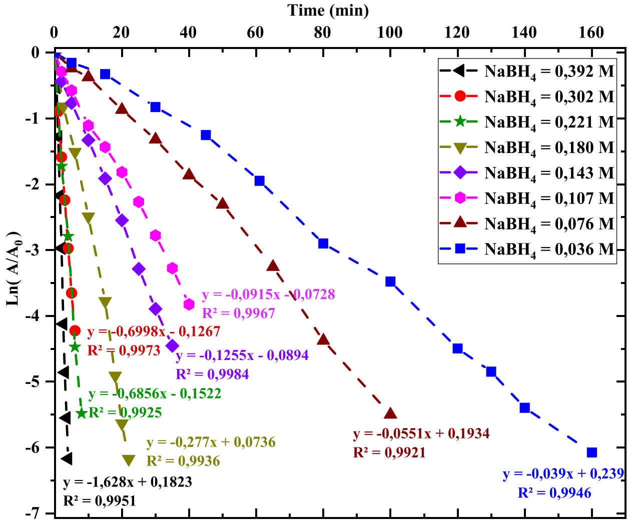

Fig. 11 Plot of $Ln(A/A_0)$ versus reaction time of 4-NP reduction in presence of various $NaBH_4$ concentrations and Co–Ag@NP nanocatalyst

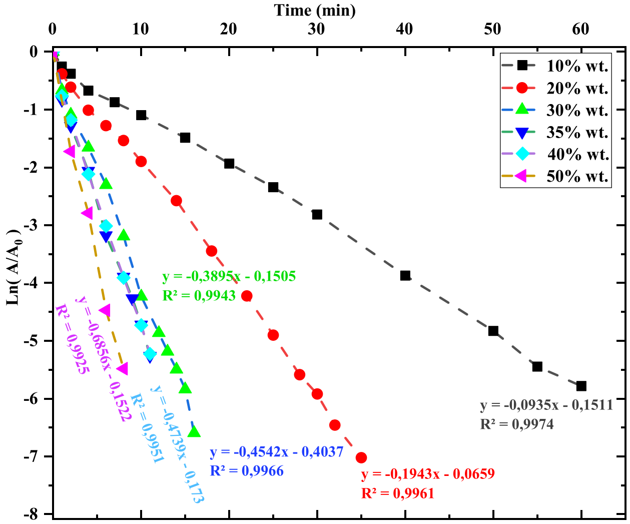

Fig. 12 Plot of $Ln(A/A_0)$ versus reaction time of 4-NP reduction by varying the Co–Ag@NP catalyst/substrate (% wt.) ratio

3.2.3 Nanocatalyst Heterogeneity and Recyclability

The heterogeneity of the nanocatalytic system was investigated according to the metal leaching during the catalytic transformation. First, the reaction was carried out in presence of Co–Ag@NP nanocatalyst and kept going for 2 min. Thereafter, the nanocatalyst was removed from the reaction mixture and then the absorbance was measured. After nanocatalyst filtration, the absorbance of 4-nitrophenolate remain constant, indicating that no reduction of 4-NP is occurred even after 120 min of reaction (Fig. S6). This result

Table 1 Co–Ag@NP catalytic performance for the reduction of various nitroarenes

Entry	Nitroarene	Aminoarene	Solvent (Water/Ethanol)	Reaction time (min)	K_{app} (min^{-1})	Conversion (%)
1	3-Nitrophenol	3-Aminophenol	Water	15	0.3037	99
2	Nitrobenzene	Aniline	7/3	120	0.0118	97
3	4-Nitrotoluene	4-Toluidine	7/3	20	0.0896	98
4	2-Nitroaniline	2-Phenilenediamine	Water	15	0.1788	90
5	4-Nitroaniline	4-Phenilenediamine	Water	15	0.0511	90
6	3-Nitrobenzaldehyde	3-Aminobenzylacohol	7/3	15	0.0657	95
7	4-Nitrobenzaldehyde	4-Aminobenzylacohol	7/3	20	0.0579	96
8	4-Nitrobenzonitrile	4-Aminobenzonitrile	7/3	30	0.0337	92
9	Methyl 3-nitrobenzoate	Methyl 3-aminobenzoate	7/3	15	0.078	94
10	3,5-Dinitrosalicylic acid	3,5-diaminosalicylic acid	Water	10	0.3063	97

Reaction conditions: nitroarene ($3.5*10^{-3}$ M), 0.221 M of $NaBH_4$ and 7 mg of Co–Ag@NP at room temperature

represents a response on the heterogeneity of the developed nanocatalyst as no silver or cobalt nanoparticles are leached into reaction mixture.

Furthermore, the catalyst stability and recyclability are the key parameters for the heterogeneous catalysts for catalytic applications. The reusability of Co–Ag@NP has been carried out for four consecutive cycles (Fig. 13). After each cycle, the nanocatalyst was recycled by decanting the aminophenol product and adding the same initial amount of 4-NP until the fourth cycle. The decantation is performed using an organic solvent. This adapted recycling method allow us to investigate the reuse of the nanocatalyst but also the reduction agent lifetime during the cycles. Hence, the recycling process is more adaptable to atom economy following green chemistry and circular economy principals. In the last cycle, a depletion of $NaBH_4$ was observed and an adequate amount of reducing agent was introduced to complete the catalytic reduction. The obtained total conversion of 4-NP during the last cycle, confirms the great efficiency in terms of catalytic stability and recyclability of Co–Ag@NP for further cycles.

To confirm the stability in terms of active sites and catalytic structure, the characterization of recycled nanocatalyst after the first and the last cycles were carried out. XRD examination of the nanocatalysts revealed that the crystallinity of the recovered Co–Ag@NP is similar to the fresh one with no-modification of active sites Ag and Co_3O_4 nanoparticles (Fig. 13b). However, SEM analyses indicate a good stability of the recycled nanocatalysts in terms of surface morphology, dispersion, and distribution of Ag and Co_3O_4 nanoparticles (Fig. 13c). Moreover, EDX spectra reveal a good stability of nanocatalysts elemental composition and confirms the stable presence of Co–Ag nanoparticles during the recyclability process (Fig. 13c).

3.2.4 Comparison of Catalytic Performance with Other Co- and Ag-Based Catalysts

A comparison of the catalytic performance of the developed Co_x-Ag_y@NP nanocatalysts with recent literature reports on 4-NP reduction catalyzed by various cobalt and silver based catalytic systems is given in Table 2.

4 Conclusion

In a summary, we have reported a successful synthesis of mono- and bimetallic Co_x–Ag_y colloidal nanoparticles and their deposition on mesoporous natural phosphate (m-NP) using wetness impregnation method. The characterizations of Co_x–Ag_y nanoparticles using UV–Visible, IR, and XRD clearly indicated the formation of Ag (0) and $Co(OH)_2$ with presence of silver oxide in the case of bimetallic Co_x–Ag_y. After the deposition of nanoparticles, all prepared Co_x-Ag_y@NP nanocatalysts were fully characterized by IR, XRD, XPS, SEM–EDX, FESEM, and TEM analyses. The structural, chemical, and physical characterizations confirmed the presence of Ag (0) and Co_3O_4 for monometallic deposition. In contrast, the Co_x–Ag_y bimetallic deposition presented a moderate amount of silver oxides due to metal synergic and redox interactions. On the other hand, the microscopic analyses revealed a stable morphology with uniform distribution and dispersion of crystalline Ag and Co_3O_4 nanoparticles on the mesoporous NP. Moreover, the Co_x–Ag_y bimetallic deposition forms silver nanospheres decorated Co_3O_4 nanograins on the surface. The prepared ex-situ nanoparticles present a core–shell form of deposited Co/Ag on m-NP surface. The catalytic performance of the prepared nanocatalysts was carried out in nitroarene reduction using $NaBH_4$, leading to pseudo-first order reaction kinetics. The excellent catalytic

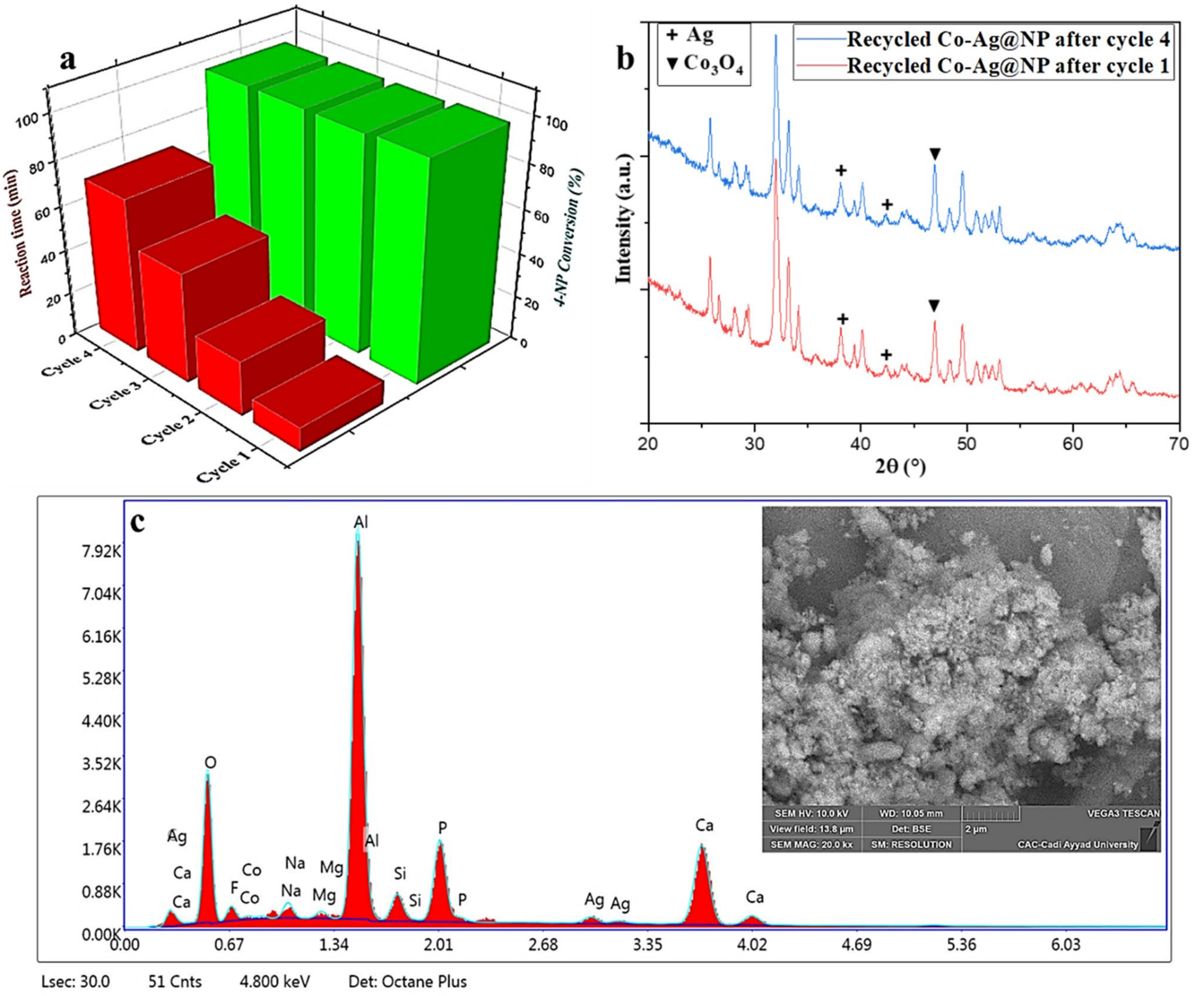

Fig. 13 Recyclability of Co–Ag@NP during 4-NP reduction: **a** Plot of the conversion and reaction time for 4 cycles, **b** XRD spectra, and **c** SEM–EDX of recycled nanocatalyst

Table 2 Comparison of catalytic performance of developed Co_x-Ag_y@NP nanocatalysts with other catalytic systems reported in literature

Catalyst	Mass (mg)	[4-NP] (mM)	[$NaBH_4$] (mM)	K_{app} (ms^{-1})	References
Pure Co	0.2	0.5	30	1.34	[57]
Ag nanodendrites	2	0.103	10	5.63	[83]
Ag@Pt/sepiolite	0.1	0.2	40	2.5	[84]
Pd-Co alloy	0.2	0.5	30	6.65	[57]
Pd@NP	1	0.5	30	0,94	[15]
Co@NP	1	0.5	30	0,54	This work
Ag@NP	1	0.5	30	4,01	This work
Co/Ag@NP	1	0.5	30	4,38	This work
Co–Ag@NP	1	0.5	30	7,57	This work

activity of bimetallic Co–Ag@NP nanocatalysts with great stability and recyclability, demonstrates the importance of metal synergy and the choice of catalyst preparation method.

Supplementary Information The online version contains supplementary material available at https://doi.org/10.1007/s10904-022-02262-8.

Funding This research did not receive any specific grant from funding agencies in the public, commercial, or not-for-profit sectors.

Declarations

Conflict of interest The authors declare that they have no conflicts of interest.

References

1. M. Akca, D. Varisli, Mol. Catal. **485**, 110823 (2020)
2. M. Domaschke, M. Schmidt, W. Peukert, J. Aerosol Sci. **126**, 133–142 (2018)
3. C. Cheephat, P. Daorattanachai, S. Devahastin, N. Laosiripojana, Appl. Catal. A Gen. **563**, 1–8 (2018)
4. F.J. Morales-Leal, J. RiveraDelaRosa, C.J. Lucio-Ortiz, D.A. DeHaroDelRío, M.A. Garza-Navarro, W. Tian, J.E. Herrera, Chem. Eng. J. **426**, 131623 (2021)
5. D. Lahiri, B. Bunker, B. Mishra, Z. Zhang, D. Meisel, C.M. Doudna, M.F. Bertino, F.D. Blum, A.T. Tokuhiro, S. Chattopadhyay, T. Shibata, J. Terry, J. Appl. Phys. **97**, 094304 (2005)
6. D. Wang, Y. Li, Adv. Mater. **23**, 1044–1060 (2011)
7. C.J. Serpell, J. Cookson, D. Ozkaya, P.D. Beer, Nat. Chem. **2011**(36), 478–483 (2011)
8. M. Moskovits, I. Srnová-Šloufová, B. Vlčková, J. Chem. Phys. **116**, 10435–10446 (2002)
9. P. Osorio-Vargas, C.H. Campos, C.C. Torres, C. Herrera, K. Shanmugaraj, T.M. Bustamante, J.N. Diaz de Leon, F. Medina, L.E. Arteaga-Pérez, Catal. Today (2021).
10. H. Jahromi, S. Adhikari, P. Roy, E. Hassani, C. Pope, T. Oh, Y. Karki, Fuel Process. Technol. **215**, 106737 (2021)
11. S. Mao, C. Wang, Y. Wang, J. Catal. **375**, 456–465 (2019)
12. A. Aberkouks, A.A. Mekkaoui, B. Boualy, S. El Houssame, M. Ait Ali, L. El Firdoussi, Adv. Mater. Sci. Eng. **2018**, 1–7 (2018)
13. A. Aberkouks, A.A. Mekkaoui, B. Boualy, S. El Houssame, M. AitAli, L. El Firdoussi, Mater. Today Proc. **13**, 453–457 (2019)
14. A. Aberkouks, A.A. Mekkaoui, M. Ait Ali, L. El Firdoussi, S. El Houssame, J. Chem. **2020**, 1–11 (2020)
15. A.A. Mekkaoui, S. Jennane, A. Aberkouks, B. Boualy, A. Mehdi, M. Ait Ali, L. El Firdoussi, S. El Houssame, Appl. Organomet. Chem. **33**, e5117 (2019)
16. A.A. Mekkaoui, A. Aberkouks, L. Fkhar, M. Ait Ali, L. El Firdoussi, S. El Houssame, Appl. Organomet. Chem. **34**, e5917 (2020)
17. D.J. Cole-Hamilton, R.P. Tooze, in: Catal. by Met. Complexes, Springer, Dordrecht, 2006, pp. 1–8.
18. D. Astruc, F. Lu, J.R. Aranzaes, Angew. Chemie Int. Ed. **44**, 7852–7872 (2005)
19. M. Kohantorabi, M.R. Gholami, Ind. Eng. Chem. Res. **56**, 1159–1167 (2017)
20. M. Aazza, H. Ahlafi, H. Moussout, C. Mounir, A. Fadel, A. Addad, J. Environ. Chem. Eng. **8**, 103707 (2020)
21. X. Xu, Y. Liu, Y. Gao, H. Li, Colloids Surf. A Physicochem. Eng. Asp. **529**, 613–620 (2017)
22. J. Speder, A. Zana, I. Spanos, J.J.K. Kirkensgaard, K. Mortensen, M. Arenz, Electrochem. Commun. **34**, 153–156 (2013)
23. M.M. Rahman, H.B. Balkhoyor, A.M. Asiri, H.M. Marwani, Microchim. Acta **183**, 1677–1685 (2016)
24. S. Kapoor, A. Sheoran, M. Riyaz, J. Agarwal, N. Goel, S. Singhal, J. Catal. **381**, 329–346 (2020)
25. V.K. Landge, S.H. Sonawane, M. Sivakumar, S.S. Sonawane, G. UdayBhaskarBabu, G. Boczkaj, Sustain. Energy Technol. Assessments **45**, 101194 (2021)
26. N. Jadbabaei, R.J. Slobodjian, D. Shuai, H. Zhang, Appl. Catal. A Gen. **543**, 209–217 (2017)
27. K. Kaneda, T. Mizugaki, Energy Environ. Sci. **2**, 655 (2009)
28. K. Kaneda, T. Mizugaki, ACS Catal. **7**, 920–935 (2017)
29. S. Basu, H.S. Samanta, J. Ganguly, Soft Mater. **16**, 7–19 (2018)
30. K. Jemal, B.V. Sandeep, S. Pola, J. Nanomater. **2017**, 1–11 (2017)
31. E. Saion, E. Gharibshahi, K. Naghavi, Int. J. Mol. Sci. **14**, 7880–7896 (2013)
32. M. Brust, C.J. Kiely, Colloids Surf. A Physicochem. Eng. Asp. **202**, 175–186 (2002)
33. M.A. Islam, M.V. Jacob, E. Antunes, J. Environ. Manage. **281**, 111918 (2021)
34. A. Waris, M. Din, A. Ali, S. Afridi, A. Baset, A.U. Khan, M. Ali, Open. Life Sci. **16**, 14–30 (2021)
35. B. Raveau, M.M. Seikh, Zeitschrift Fur Anorg. Und Allg Chemie **641**, 1385–1394 (2015)
36. S.M. Ansari, R.D. Bhor, K.R. Pai, D. Sen, S. Mazumder, K. Ghosh, Y.D. Kolekar, C.V. Ramana, Appl. Surf. Sci. **414**, 171–187 (2017)
37. G. Chai, W. Zhang, L.F. Liotta, M. Li, Y. Guo, A. Giroir-Fendler, Appl. Catal. B Environ. **298**, 120606 (2021)
38. Y. Feng, Z. Li, C.-Q. Cheng, W.-J. Kang, J. Mao, G.-R. Shen, J. Yang, C.-K. Dong, H. Liu, X.-W. Du, Appl. Catal. B Environ. **299**, 120658 (2021)
39. B. Guo, J. Ma, Y. Shi, K. Zheng, M. Wu, G. Ren, S. Komarneni, Ceram. Int. **47**, 27617–27623 (2021)
40. J. Iqbal, A. Numan, R. Jafer, S. Bashir, A. Jilani, J. Alloys Compd. 821 (2020) 153452.
41. J. Iqbal, A. Numan, M. OmaishAnsari, R. Jafer, P.R. Jagadish, S. Bashir, P.M.Z. Hasan, A.L. Bilgrami, S. Mohamad, K. Ramesh, S. Ramesh, Polymers (Basel). **12**, 2816 (2020)
42. H.M.A. Amin, C.J. Bondue, S. Eswara, U. Kaiser, H. Baltruschat, Electrocatalysis **8**, 540–553 (2017)
43. A. Ashok, A. Kumar, Int. J. Hydrogen Energy **46**, 4788–4797 (2021)
44. A. Ashok, A. Kumar, M.A. Matin, F. Tarlochan, ACS Omega **3**, 7745–7756 (2018)
45. P. Hervés, M. Pérez-Lorenzo, L.M. Liz-Marzán, J. Dzubiella, Y. Lu, M. Ballauff, Chem. Soc. Rev. **41**, 5577 (2012)
46. T. Aditya, A. Pal, T. Pal, Chem. Commun. **51**, 9410–9431 (2015)
47. G. Booth, in: Ullmann's Encycl. Ind. Chem., Wiley-VCH Verlag GmbH & Co. KGaA, Weinheim, Germany, 2000.
48. J.C. Oxley, in: Explos. Eff. Appl., Springer New York, New York, NY, 1998, pp. 137–172.
49. G. Eichenbaum, M. Johnson, D. Kirkland, P. O'Neill, S. Stellar, J. Bielawne, R. DeWire, D. Areia, S. Bryant, S. Weiner, D. Desai-Krieger, P. Guzzie-Peck, D.C. Evans, A. Tonelli, Regul. Toxicol. Pharmacol. **55**, 33–42 (2009)
50. Q. Wang, W. Jia, B. Liu, A. Dong, X. Gong, C. Li, P. Jing, Y. Li, G. Xu, J. Zhang, J. Mater. Chem. A **1**, 12732 (2013)
51. Ö. Metin, H. Can, K. Şendil, M.S. Gültekin, J. Colloid Interface Sci. **498**, 378–386 (2017)
52. J. Zhang, G. Chen, D. Guay, M. Chaker, D. Ma, Nanoscale **6**, 2125–2130 (2014)
53. V.K. Harika, H.K. Sadhanala, I. Perelshtein, A. Gedanken, Ultrason. Sonochem. **60**, 104804 (2020)

54. Y. Wang, Q. Li, P. Zhang, D. O'Connor, R.S. Varma, M. Yu, D. Hou, J. Colloid Interface Sci. **539**, 161–167 (2019)
55. H. Chen, X. Fan, J. Ma, G. Zhang, F. Zhang, Y. Li, Ind. Eng. Chem. Res. **53**, 17976–17980 (2014)
56. A.D. Verma, S. Pal, P. Verma, V. Srivastava, R.K. Mandal, I. Sinha, J. Environ. Chem. Eng. **5**, 6148–6155 (2017)
57. T.A. Revathy, T. Sivaranjani, A.A. Boopathi, S. Sampath, V. Narayanan, A. Stephen, Res. Chem. Intermed. **45**, 815–832 (2019)
58. H. Göksu, H. Can, K. Şendil, M.S. Gültekin, Ö. Metin, Appl. Catal. A Gen. **488**, 176–182 (2014)
59. H. Göksu, S.F. Ho, Ö. Metin, K. Korkmaz, A. MendozaGarcia, M.S. Gültekin, S. Sun, ACS Catal. **4**, 1777–1782 (2014)
60. Ö. Metin, A. Mendoza-Garcia, D. Dalmızrak, M.S. Gültekin, S. Sun, Catal. Sci. Technol. **6**, 6137–6143 (2016)
61. Natural Phosphate (NP) Comes from Khouribga Region (Morocco); It Is Readily Available (Raw or Treated) from the Centre for Studies and Research of Mineral Phosphates (CERPHOS) 37, Bd My Ismail, Casablanca, Morocco
62. T. Chaieb, L. Delannoy, C. Louis, C. Thomas, Catal. Lett. **146**, 2622–2629 (2016)
63. M. Medvidović-Kosanović, A. Stanković, M. Jozanović, M. Drulak, M. Ilić, Croat. Chem. Acta **91**, 421–426 (2018)
64. J.C. Villegas, O.H. Giraldo, K. Laubernds, S.L. Suib, Inorg. Chem. **42**, 5621–5631 (2003)
65. L.-H. Su, X.-G. Zhang, C.-H. Mi, B. Gao, Y. Liu, Phys. Chem. Chem. Phys. **11**, 2195 (2009)
66. R. Xu, H.C. Zeng, J. Phys. Chem. B **107**, 12643–12649 (2003)
67. M. Aghazadeh, H.M. Shiri, A.-A.M. Barmi, Appl. Surf. Sci. **273**, 237–242 (2013)
68. J. Wang, Y. Bao, C. Cui, Z. Zhang, S. Li, J. Pan, Y. Zhang, G. Tu, J. Wang, Z. Li, J. Mater. Sci. **54**, 7692–7701 (2019)
69. M. Aghazadeh, Int. J. Electrochem. Sci. **12**, 5792–5803 (2017)
70. R. Li, Z. Hu, X. Shao, P. Cheng, S. Li, W. Yu, W. Lin, D. Yuan, Sci. Rep. **6**, 18737 (2016)
71. A.I. Oje, A.A. Ogwu, M. Mirzaeian, N. Tsendzughul, J. Electroanal. Chem. **829**, 59–68 (2018)
72. A.V. Salker, M.S. FalDesai, Catal. Sci. Technol. **6**, 430–433 (2016)
73. D.D.M. Prabaharan, K. Sadaiyandi, M. Mahendran, S. Sagadevan, Appl. Phys. A **123**, 264 (2017)
74. P. Scherrer, Nachrichten Math. Phys. **2**, 98–100 (1918)
75. A. Al-Sarraj, K.M. Saoud, A. Elmel, S. Mansour, Y. Haik, S.N. Appl, Sci. **3**, 15 (2021)
76. V. Rico-Pérez, A. Bueno-López, Appl. Sci. **4**, 468–481 (2014)
77. H. Romar, E. Rivoire, P. Tynjälä, U. Lassi, Top. Catal. **60**, 1408–1414 (2017)
78. P. Prieto, V. Nistor, K. Nouneh, M. Oyama, M. Abd-Lefdil, R. Díaz, Appl. Surf. Sci. **258**, 8807–8813 (2012)
79. A. Sarnecki, P. Adamski, A. Albrecht, A. Komorowska, M. Nadziejko, D. Moszyński, Vacuum **155**, 434–438 (2018)
80. A.M. Ferraria, A.P. Carapeto, A.M. Botelho do Rego, Vacuum **86**, 1988–1991 (2012)
81. J. Hidalgo-Carrillo, J. Sebti, A. Marinas, J.M. Marinas, S. Sebti, F.J. Urbano, J. Colloid Interface Sci. **382**, 67–73 (2012)
82. B. Baruah, G.J. Gabriel, M.J. Akbashev, M.E. Booher, Langmuir **29**, 4225–4234 (2013)
83. W. Zhang, F. Tan, W. Wang, X. Qiu, X. Qiao, J. Chen, J. Hazard. Mater. **217–218**, 36–42 (2012)
84. Y. Ma, X. Wu, G. Zhang, Appl. Catal. B **205**, 262–270 (2017)